

# Mineralogical mapping using EO-1 Hyperion data for iron mine identification

Wejden Bouzidi<sup>1</sup>,<sup>a,\*</sup> Nouha Mezned<sup>1</sup>,<sup>a,b</sup> and Sâadi Abdeljaoued<sup>a</sup>

<sup>a</sup>University of Tunis El Manar, Department of Geology, Laboratory of Mineral Resources and Environment, Faculty of Sciences of Tunis, Tunis, Tunisia

<sup>b</sup>University of Carthage, Higher Institute of Preparatory Studies in Biology and Geology of Soukra, Institution of Agricultural Research and Higher Education, Tunis, Tunisia

**Abstract.** The Tamera open pit mine is located in the Nefza mining district (north-west of Tunisia) where the reddish soil reveals its strong potential for heavy Fe mineralization, along with other metals (Pb, Zn, and Mn). This study explored Iron oxide mineralization in a particular nappe zone using multiscale field visible and near infrared/short waves infrared and EO-1 Hyperion hyperspectral data. Thus, spectral features fittings were conducted on Hyperion data for mineral mapping using scene-extracted endmembers. A first minimum noise fraction algorithm was used to reduce the hyperspectral data's dimensionality, followed by the Pixel Purity Index and  $n$ -dimensional visualization to extract the pure pixels (endmembers) from the cluster of pixels in the data cube. Furthermore, 56 soil samples were collected from the test site and spectrally measured using Analytical Spectral Devices FieldSpecHiRes spectrometer, which covers the spectral range between 350 and 2500 nm. All samples were analyzed in the laboratory with x-ray diffraction. Endmember extracted spectra were compared with field measurements before EO-1 Hyperion processing. Mapping results revealed the occurrence of a mineralogy composition consisting particularly of iron oxide minerals (hematite and goethite) and bearing minerals, such as clays (kaolinite), within all samples. © The Authors. Published by SPIE under a Creative Commons Attribution 4.0 International License. Distribution or reproduction of this work in whole or in part requires full attribution of the original publication, including its DOI. [DOI: [10.1117/1.JRS.16.024514](https://doi.org/10.1117/1.JRS.16.024514)]

**Keywords:** Hyperspectral spectroscopy; EO-1 Hyperion data; SFF; XRD analysis; iron ore characterization; oxide mineral mapping.

Paper 210708G received Nov. 2, 2021; accepted for publication Apr. 25, 2022; published online May 19, 2022.

## 1 Introduction

Tunisian iron minerals mainly include Fe oligist (hematite), goethite, and stilpnosiderite. These three minerals make up almost all exploitable minerals and are accompanied by traces of magnetite, lepidocrocite, and various impurities varying with the deposits.<sup>1</sup> In Tunisia, two types of ores can be distinguished, an oolitic sedimentary deposit (Jebel Ank) and epithermal deposits, with the following aspects among them:

1. Northern deposits are considered to be the result of the substitution of Pontian sediments by iron oxides, and they appear to be related to underlying Blende–Pyrite–Galena deposits.
2. Central Tunisia's deposits are mixed, vein, and substitute deposits in limestones generally of aptian age.
3. Gossans can also be distinguished from varied deposits. The first type can be related to Harraba, I'Hameima, Slata, Jerissa, Nebeur, the Bellouta, the Mrhila, and the Chambi. The second type of epithermal deposits belongs to the mines of Ras Rajel, Moktael Hadid BouLanague, Tamera-Ganara-El Harech, and Douahria, which are located in the Nefza district and are considered to be a major contribution to the iron supply in the north of Tunisia.

---

\*Address all correspondence to Wejden Bouzidi, [wejdenbouzidi22@gmail.com](mailto:wejdenbouzidi22@gmail.com)

The ferriferous formations in these epithermal basins are spatially and temporally associated with the Middle to Late Miocene magmatism of the Nefza district, mainly the Haddada rhyolite complex in the enigmatic Oued Belief structure.<sup>2,3</sup> The regolith of the Tamera mining site has been mentioned for its variability in the grade of iron oxide and hydroxide bearing minerals that are successfully and economically extracted.<sup>2,3</sup>

Given the economic interest of the Neogene basins of different iron mineralization structures, strategic mining exploration constitutes a preliminary phase throughout the exploitation cycle of these raw materials.<sup>2</sup> This stage of regional reconnaissance requires intensive field exploration to understand the geological context through lithological mapping and to identify surface showings that can help focus the work. Mining exploration has been carried out using a variety of techniques based on classical methods to determine the nature and distribution of geological units and exploration targets for economic minerals, but these traditional methods remain heavy-handed techniques that produce discontinuities in point and time information at each sampling point and are time consuming and expensive.

According to previous studies, remote sensing images can be successfully used to locate the assemblage of hydrothermal alteration minerals such as iron minerals, silica, clay, calcite, jarosite, and alunite.<sup>4,5</sup> Several geoscientists have used multispectral, hyperspectral, and *in situ* data remote sensing methods because of broad hydrothermal alteration, through image enhancement, spectral analysis, and band ratio techniques.<sup>6-19</sup> These minerals are indicators of different alteration zones, and their identification can provide direct evidence of mineralization.<sup>6,20-27</sup>

Ref. 28 conducted a comprehensive evaluation of multi- and hyperspectral geologic remote sensing to show the utility of remote sensing for mineral mapping. However, acquiring these data sets is often very difficult, incurs a relatively high cost per data acquisition, and has limited availability. Hyperspectral bands could provide abundant information about many important earth-surface minerals. The visible and near infrared (VNIR) region is useful for discriminating minerals exposed at gossans, such as goethite, hematite, and jarosite. The short-wave infrared (SWIR) region covers spectral features of hydroxyl-bearing minerals as well as C–O bearing minerals such as phyllosilicates, sulfates, and carbonates, which are common to many geologic rock units and hydrothermal alteration assemblages.<sup>29,30</sup> The SWIR region provides spectral information about most of the diagnostic altered minerals. As a result of hyperspectral data's vast amount of spectrum information and higher spectral resolution, mineral identification can now be done with a much higher level of precision. Hyperion data for geological mapping has been researched, validated, and proven in several studies throughout the world.<sup>27,31-40</sup>

Many successful studies have shown the usefulness of multispectral and hyperspectral images for mineral mapping.<sup>41-43</sup> Ref. 44 showed that hyperspectral radiometric approaches might be utilized instead of the traditional way to construct models to assess the concentration of iron minerals in iron ores of Noamundi and Joda Mines, Eastern India. Ref. 42 used the Hyperion image, field, and laboratory-based spectroscopy for assessing the grades of iron ores in the Noamundi area, Eastern India. The ASTER imaging data was used by Ref. 43 for their potential to provide important information relevant to the delineation of iron deposits in Kanjamalai, Godumalai, and Nainarmalai, Tamilnadu, India. A ratio technique was implemented and validated using laboratory results. Findings showed a correlation with their corresponding locations in the image.<sup>43</sup> Ref. 9 used ASTER SWIR data for sub-pixel mapping of alteration minerals around the iron-rich mineral occurrences of the Tamera mine and Pb-Zn wastes of Sidi Driss.

Therefore, this work is intended, for the first time in Tunisia, to decipher the potential of *in situ* spectral remote sensing and digital processing of Hyperion data and to identify and characterize the iron ores' depositional mapping in the northern Tamera mine site. As the present work was conducted on a forested area, both continuum removal and band ratio methods were applied for the empirical detection of the groups of iron-bearing minerals that show strong absorption bands at similar wavelengths.<sup>40</sup> Furthermore, a spectral feature fitting was implemented to map the alteration minerals, coupled with comprehensive hyperspectral spectroscopy and x-ray diffraction (XRD) laboratory analyses.

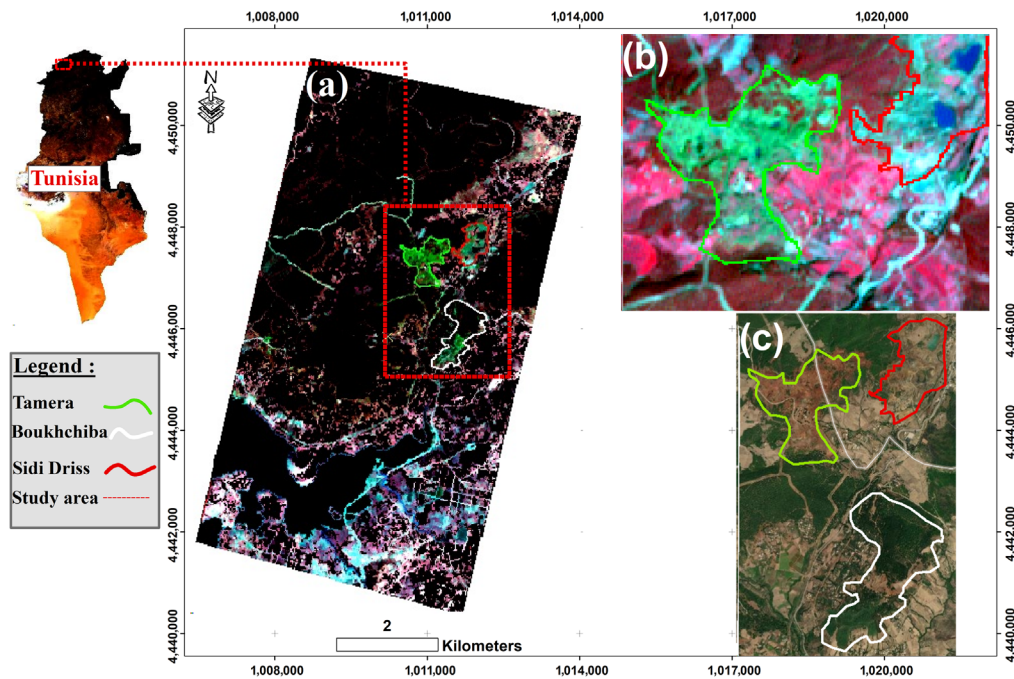


**Fig. 1** Study region considered for the iron investigation: (a) false color composition (FCC) of Hyperion combination (band 40, 31, and 13) (full scene  $360 \times 250 \times 1$ ), (b) FCC of ASTER VNIR data ( $107 \times 66 \times 9$  pixels), (c) surface exposure of iron ore alteration zone (Tamera, Sidi Driss, and Boukhchiba) on Google Earth Imagery.

## 2 Study Site

The study area ( $37^{\circ}3.318'N$ ,  $9^{\circ}6.43'E$ ) is situated in the north-west of the Oued Belief volcano-sedimentary complex (Belt), 120 km NW of the city of Tunis, 30 km to the east of the town of Tabarka, and 10 km north of Nefza province (Fig. 1). The Nefza region is characterized by high vegetation and a tropical microclimate environment with an average rainfall of about 100 mm/year.

In the middle of the century, this province was known as a mining district center because of its tremendous economic potential of ore deposit and different Pb-Zn and Fe mineralization indexes. It is part of the widespread northern Tunisian “Nappe zone,”<sup>2,3</sup> composed of thrust sheets. The small post-nappe basins, ranging from the Messinian to Pliocene in age and generally located near magmatic rocks, host Fe and Pb-Zn ores. The Pb-Zn sulfide ore relating to these post-nappe basins is observed at Sidi Driss and consists of galena and sphalerite associated with As-bearing marcasite, pyrite, barite, and celestite.

The Sidi Driss is partly overlain by the younger Mio-Pliocene basin, in which heavily Fe-mineralized sediments (Tamera formation) overlie the Sidi Driss formation, which is, in turn, composed of ferruginous pyroclastic deposits<sup>45-48</sup> (Fig. 2).

From the outside to the center of Oued Belief’s complex structure (Fig. 3), we can see a primary edge breccia creating a belt, mainly East North East-West South West, along the axis of the elliptical shape (6 km by 3 km).<sup>3</sup> The secondary Breccia can take the form of large plages aligned along accidents with a subparallel direction to that of the edge breccia, for example, the west sector of Boukhchiba, or of scattered blocks preferentially located upstream of N-S trending discontinuities, for example, the block near the granodiorite. The ferruginous breccia of the margin and those of the interior, overall, have little morphological differences: they are all extremely cemented sheaths. They produce projections over the entire structure and are missing in the river-cut low parts<sup>2,46,47</sup> (Fig. 3). They are distinguished by the size of their elements, which varies depending on their placement. The ferruginous bodies of Boukhchiba, Raget Ouled Mariem, and Kef Salem are encased in large lenses brecciated at the base, whereas the summit horizons, surface alteration, and pedogenesis have formed banks and layers intercalated in ferruginous silts,

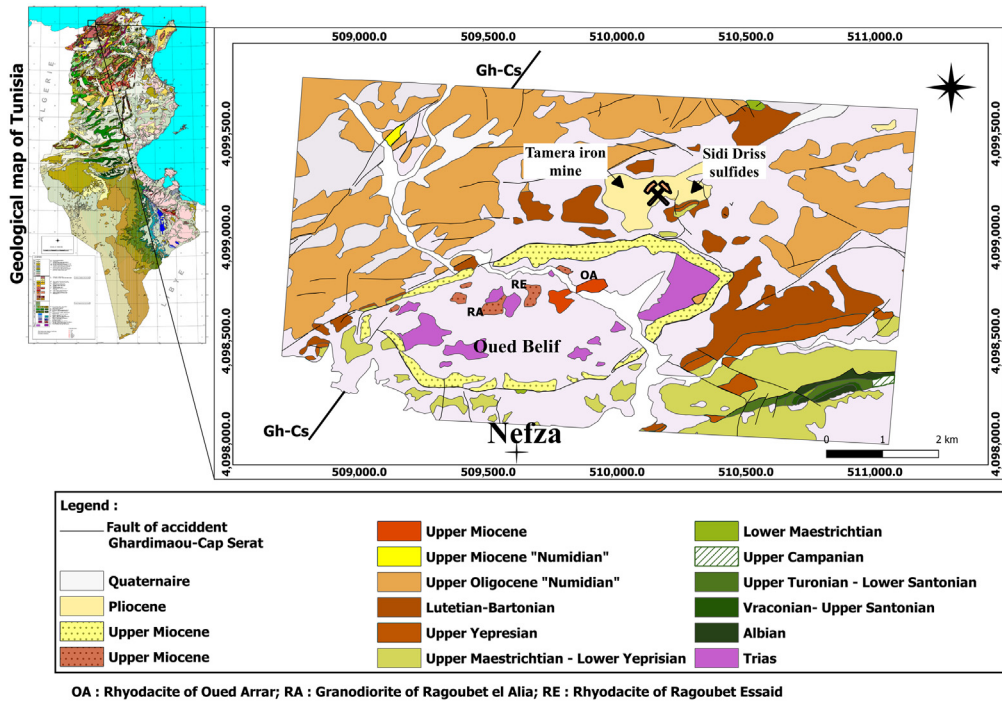


**Fig. 2** Digitized extract of the geological map of the mining district of Nefza focusing on the Oued Belief caldera hydrothermal field (scale 1:25,000) (modified based on Refs. 49, 50).

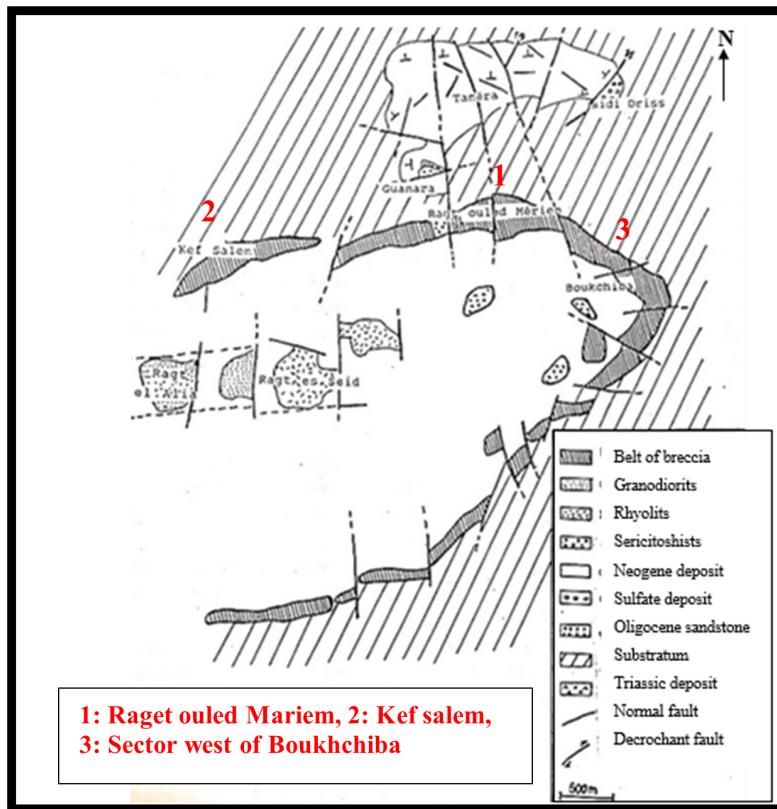


**Fig. 3** Structural map of the study area.<sup>3</sup>

causing concentrations of centimetric to decametric iron. Fractures as well as syn-deposit fractures are filled with hydrothermal clays.<sup>1,3,45,46</sup>

### 3 Materials and Methods

#### 3.1 Field Sampling and Laboratory Analysis

A sampling campaign was conducted between March and April 2017 in Nefza to define the diverse lithological facies at the level of iron mining sites: the site of Tamera, the Pb-Zn mine of Sidi Driss, and the abandoned site of Boukhchiba. Climatic conditions were excellent during the sampling, with clear weather locally supplemented by some cloudy arrivals that became more varied to quite dense on several days.

A layer of 0.5 to 1.5 cm was scraped from the surface for each of the 65 samples collected as follows: 20 surface samples for the “Tamera” iron mine site, 20 surface samples for the Sidi Driss Pb-Zn mining site, and 16 surface samples for the “Boukhchiba” iron mining site. All selected samples were then reduced to a powder size of more than 2 mm in an agate mortar and analyzed by XRD for the identification of minerals on a PANalyticalX’Pert Pro diffractometer and the estimation of their respective abundance (Fig. 4).

#### 3.2 Hyperspectral Field Data

*In situ* spectroradiometric hyperspectral measurements were acquired using the Analytical Spectral Devices (ASD) FieldSpecHiRes spectrometer, which operates in a full range between 350 and 2500 nm to provide a prior knowledge of geology. Aiming for maximum solar lighting, all measurements were conducted between 10 and 2  $\mu\text{m}$ . Latitude and longitude coordinates of all measured samples were recorded using a portable global positioning system (Fig. 5).

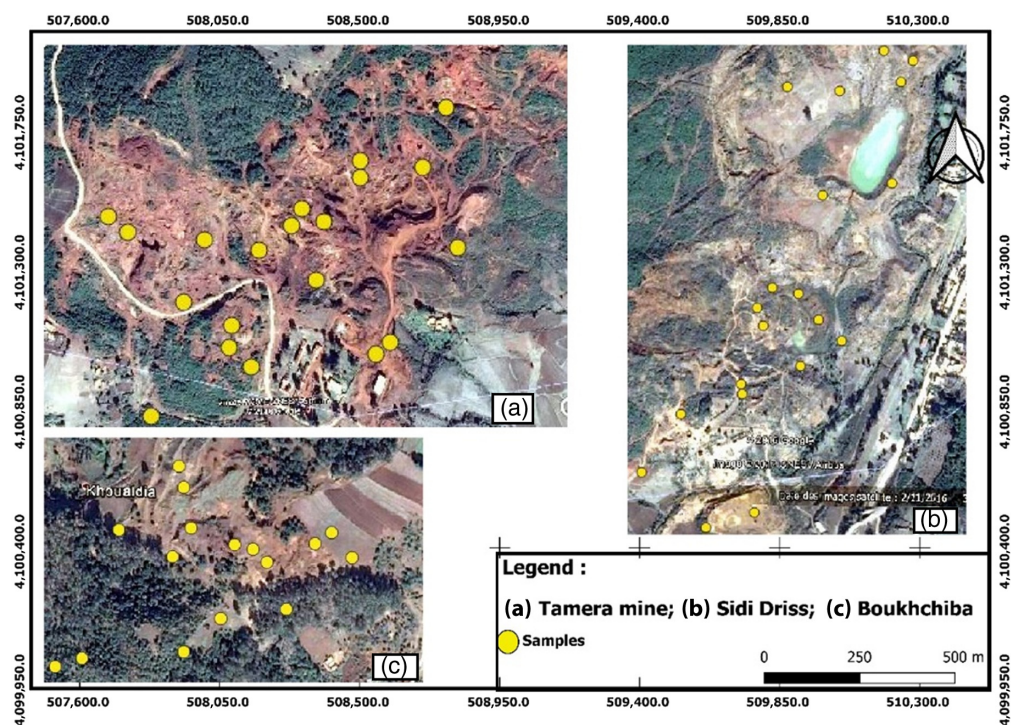


**Fig. 4** Map showing the localization of collected samples in the three sites: (a) Tamera, (b) Sidi Driss, and (c) Boukhchiba.

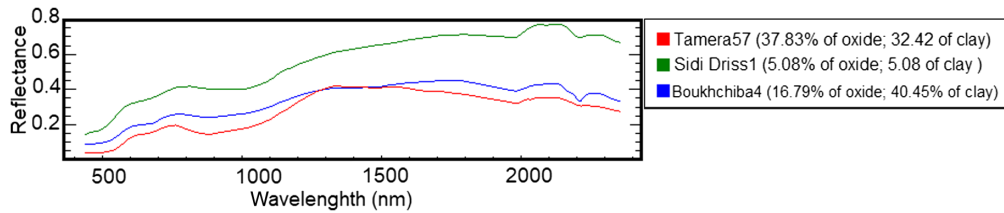


**Fig. 5** Examples of field spectra measured *in situ*.

**Table 1** A description of the Hyperion data used in this research.

Attributes	Hyperion data
Entity ID	EO1H1920342003084110PZ_B001_L1GST.TIF
Acquisition date	March 25, 2003
Acquisition time	09:51:09
Sun azimuth	140.823494
Sun elevation	48.173579
Spatial resolution	30 m

### 3.3 EO-1 Hyperion Imagery Data

In the framework, simultaneous to the field camping period, we used hyperspectral Hyperion data for iron ore mapping in the Nefza district. “Environment for Visualizing Images” (ENVI) 5.1 software package was used to process the Hyperion, Level 1T dataset scenes that took place on March 25, 2003 (Table 1). The choice of the scene used is justified by its good quality with a lower density of cloud cover as well as the seasonal coincidence between its acquisition date and the field campaign to maintain the same meteorological conditions. Moreover, the scene of the March 25, 2003, is the only one that covers the entire study area. The hyperspectral remote sensing satellite, EO-1 Hyperion, was launched in November 2000 with two spectrometers in VNIR and SWIR covering the wavelength range of 400 to 2500 nm with 242 bands of approximately 10 nm spectral bandwidth and 30-m spatial resolution.<sup>51</sup> The VNIR (VIS + NIR) detector covers the range of 400 to 900 nm in 40 channels and the SWIR detector covers a range of 1000 to 2500 nm in 172 channels.<sup>52</sup>

### 3.4 Methodology

The proposed methodology consists of two main parts, namely, the preprocessing of the datasets and the main processing. The flowchart of the methodological steps followed in this study is presented in Fig. 6.

#### 3.4.1 Preprocessing

**Hyperion image atmospheric and geometric corrections.** Pre-processing steps included the removal of overlapping and inactive bands (1 to 7, 58 to 78, and 225 to 242).<sup>53</sup> Only 153 bands were used for radiometric calibration after suppressing the bad bands. The surface reflectance was derived after that from the radiance data. Both atmospheric and geometric corrections were processed using the ENVI 5.1 software to remove noise and acquire surface reflectance. The fast line of sight atmospheric analysis of hyperspectral cubes atmospheric correction algorithm was used to correct the absorption and scattering effects. Finally, after the low signals and noisy channels were removed, a resulting Hyperion image with 153 bands was used for this study.

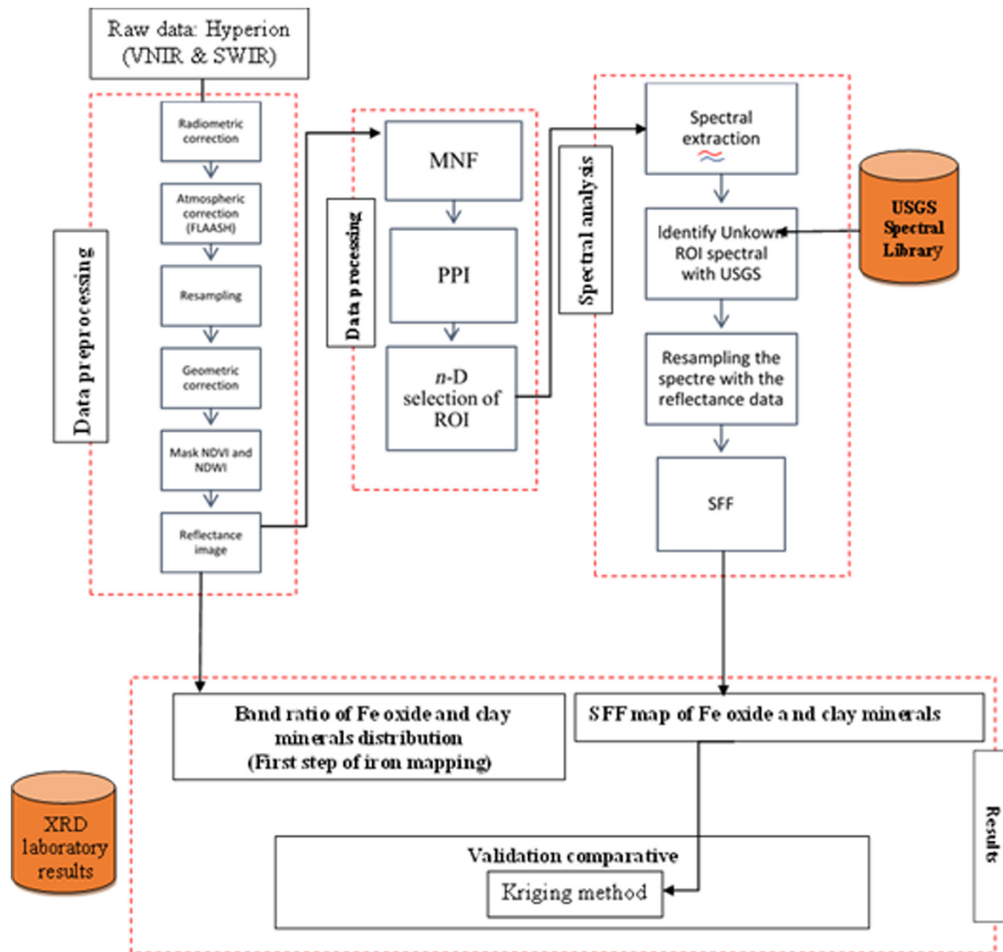


Fig. 6 Flow chart of the methodology followed in this study.

*Hyperion image enhancement.* The band rationing was widely used as a simple enhancement technique in remote sensing analysis. It has been used to emphasize the anomaly of target alteration minerals that have absorption features in certain wavelengths, such as iron and clay indexes, for instance, which have absorptions around 550, 660, 760, 800, 860, 1600, 1700, 2167, and 2203 nm wavelength regions, respectively.<sup>54-56</sup>

Geological mapping has benefited from the band ratio technique in several studies,<sup>57</sup> particularly when using hyperspectral imagery data.<sup>39</sup> In this study, the band ratio based on Hyperion data successfully delimited iron ore zones in Tamera, which contain ferric and ferrous oxide minerals as well as bearing minerals.

Both indices were calculated for semi-automatic mapping of ferric iron oxides and clays in the iron ore deposits in the three selected areas, using the equations

$$\text{Ferric iron oxide} = (b_{23}/b_{13}), \quad (1)$$

$$\text{Clays} = (b_{134} \times b_{138}/b_{1482}), \quad (2)$$

where  $b$  refers to band, and band 13, band 23, band 134, band 138, and band 148 refer to 559, 660, 2163, 2203, and 2309 nm, respectively [Figs. 7(a) and 7(b)]. This approach is based on using mineral indices (clay mineral and iron oxide) as well as normalized difference vegetation indices (NDVI) and Normalized Difference 860/1240 Normalized Difference Water Index (NDWI), which are computed using the equations

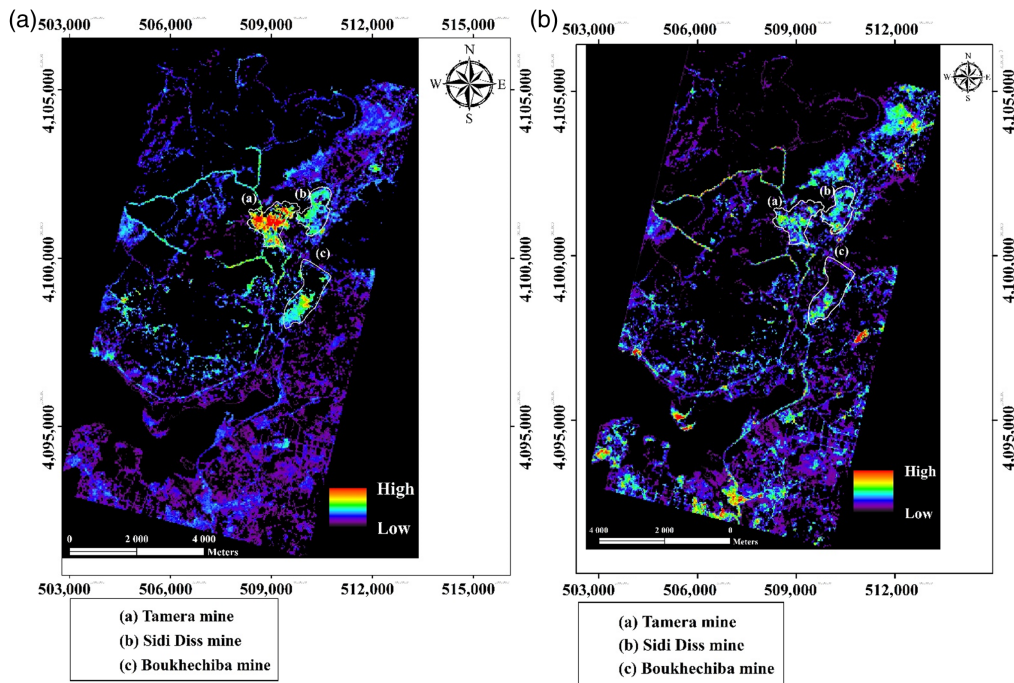


**Fig. 7** Maps (full scene:  $360 \times 250 \times 1$  pixels) showing the calculated indices using Hyperion data acquired on the Tamera mine site: (a) ferric oxide index ( $b_{23}/b_{13}$ ) and (b) clay index ( $b_{134} \times b_{138}/b_{148}^2$ ).

$$\text{NDVI} = (\rho_{\text{red}} - \rho_{\text{NIR}}) / (\rho_{\text{red}} + \rho_{\text{NIR}}), \quad (3)$$

$$\text{NDWI} = (860 \text{ nm} - 1240 \text{ nm}) / (860 \text{ nm} + 1240 \text{ nm}), \quad (4)$$

where  $\rho_{\text{red}}$  and  $\rho_{\text{NIR}}$  refer to red band surface reflectance and near infrared band surface reflectance, respectively. The NDVI was calculated, and the respective mask was applied to exclude pixels with dense vegetation from further processing and thus to emphasize the geological interpretation.

### 3.4.2 Main processing

**MNF transformation.** With regard to image quality, the minimum noise fraction (MNF) transform used in this study is capable of supplying excellent high to low order to the bands. MNF specifies how geographical information can be used to interpret the signal and noise covariance structure.<sup>58</sup> The MNF procedure was implemented to decrease the dimensionality of Hyperion data by suppressing noise. It is also useful for displaying variance within the data set.<sup>59</sup> In the first eigen value image, there is a bright gradient with a significant smile. To reduce spatial noise, the MNF was employed to separate uncorrelated noises.<sup>59</sup> In general, the first few MNF bands communicate the most significant information, whereas the subsequent bands become increasingly noisy. Noise is often present in MNF bands with computed eigen values below one.<sup>60</sup>

It was decided to save just 10 of the MNF bands and turn them into reflectance data. The resulting reflectance dataset contained 153 bands, but only with the spectral information of the chosen MNF bands.

**Endmember extraction.** For more than two decades, many methods for endmember bundle extraction from hyperspectral images have been proposed,<sup>61,62</sup> with many of them extracting endmembers from each subregion of the original image and then clustering the extracted endmembers to generate endmember bundles, which means that each feature's endmembers are

represented by a collection including numerous spectra.<sup>63</sup> When the subregion contains no pure pixels, however, the experiment methods may extract mixed pixels as possible endmembers. The researchers used Pixel Purity Index (PPI)<sup>64</sup> to assess the purity of candidate endmembers to overcome these concerns. In this paper, the PPI algorithm is used to extract the pure pixels of oxide and clay minerals.

Spectral endmembers were extracted from Hyperion imagery using a combination of the MNF, PPI, and  $n$ -dimensional visualizer technique.<sup>65,66</sup> The PPI is calculated by projecting  $n$ -D scatter plots onto a random unit vector many times. In each projection, ENVI maintains track of the extreme pixels (those at the ends of the unit vector), as well as how many times each pixel has been designated as extreme in all of the projections (ENVI user guide 2003). During the region of interest's (ROI) selection, which is geologically known,<sup>67,68</sup> the highest pixel values are used to compute the  $n$ -dimensional visualization. To extract the pure pixels and determine their spectra, the  $n$ -dimensional visualization is applied to MNF images. The extracted spectra were characterized using the spectral analysis procedure available at ENVI.

**Spectral feature fittings.** In this study, we used the spectral feature fittings (SFF) method based on the comparison of spectra with a mineral reference spectrum and the estimation of the root mean square error (RMSE). A low RMSE and a high scale factor value indicate that the minerals are closely matched. The RMSE image quantity and the condition scale will be equal.<sup>44,69-71</sup> The continuum removal was applied before creating scaled images, which is given by

$$\text{Scr} = S/C, \quad (5)$$

where Scr is the continuum-removed spectra,  $S$  is the original spectra, and  $C$  is the continuum curve.

Steps in SFF include creating a scale image and an RMS error image, or RMSE. After subtracting the continuum, which removed one spectrum at a time from the image, scale images were created. Using the scale image, each pixel's absorption feature can be predicted and measured. The scale factor, which is calculated by comparing bands to bands using the least-square fit procedure, measures the abundance of spectral features. A higher scale factor value correlates with a higher mineral absorption rate.<sup>72</sup> According to the brightness of the scale picture, the image spectrum was more closely aligned with the reference spectra of minerals in the pixel than what was previously believed. A low RMSE and a high scale factor value indicate that minerals are closely matched. RMSE image quantity and condition scale were thus equal.

## 4 Results and Discussion

### 4.1 Mineralogical Composition

The XRD results show high levels of hematite and goethite within Tamera samples. Other minerals were mainly identified through the mineral composition such as quartz and clays minerals. Feldspath, sulphate minerals (barite and gypsum), and sulfide minerals such as galena were, however, identified as accessory minerals. Jarosite was found within only nine samples, indicating that this iron sulfate mineral is -significantly non-existent [Fig. 8(a)]. The mineralogical results of the Sidi Driss samples show high levels of quartz due to the lithological nature of Sidi Driss series. Moreover, except the presence of quartz, XRD results revealed the existence of a similar mineralogical composition containing mainly clay minerals, hematite, goethite, and sulphate minerals (barite and gypsum) [Fig. 8(b)]. Specifically, the Boukhchiba iron mine, shows the highest concentration values of clay minerals (kaolinite ( $d = 7.185 \text{ \AA}$ )), which was estimated to be around 50% [Fig. 8(b)].

### 4.2 Fe Mineralization Surface Spectra

The presence of oxides and hydroxides was revealed through all of the measured spectra in the three sites. Both important absorption features were represented by approximately 0.520 and

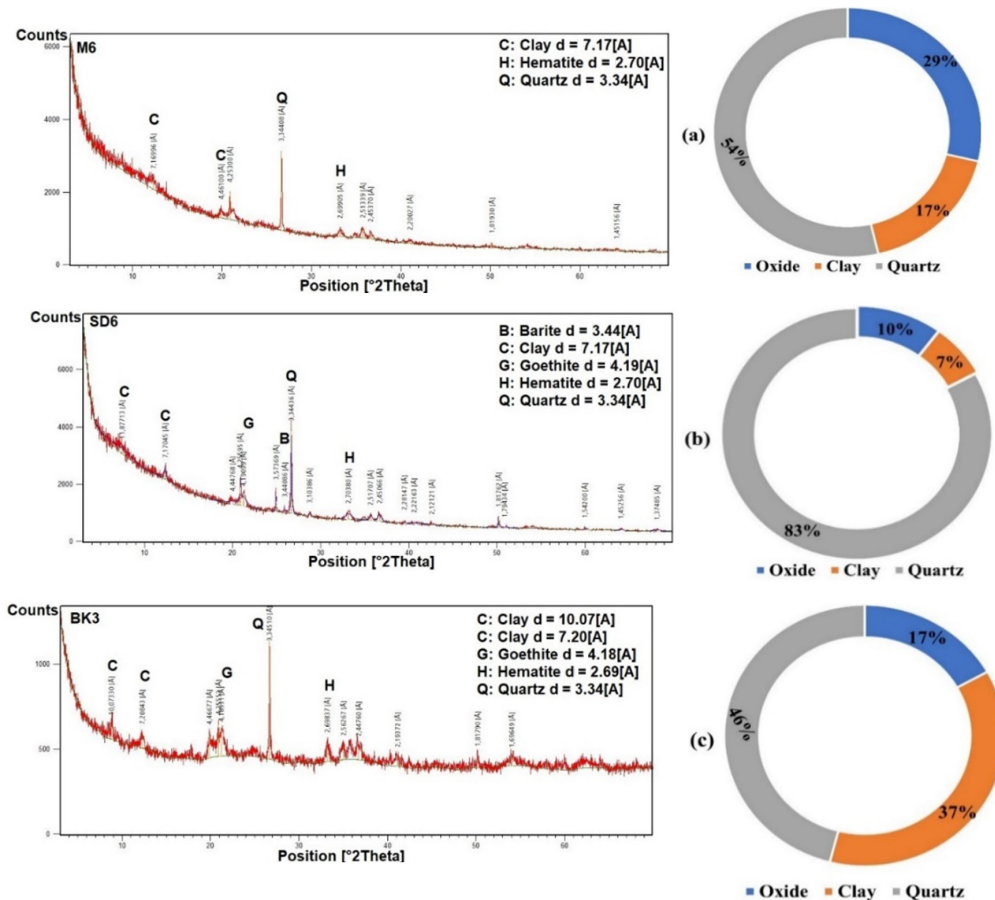


**Fig. 8** X-ray diffractogram ('*d*' values [Å]) of soil samples with their histogram of mean abundances (%) of iron and clay minerals in the three sites: (a) Tamera iron mine, (b) Sidi Driss Pb-Zn mine, and (c) Boukhchiba iron mine.

0.890  $\mu\text{m}$ , which were reciprocally proportional and related to the presence of ferric iron ( $\text{Fe}^{3+}$ ).<sup>73</sup> The presence of jarosite was not revealed through all soil sample spectra.<sup>39</sup> For total clays, absorption peaks were expected to approximately be within the SWIR region at 2.206  $\mu\text{m}$ , due to the combination of OH and OH-Al bending.<sup>25,39,73</sup> The ASD spectra matched the laboratory results (Fig. 9).

The existence of ferric iron and clay minerals was verified by comparing measured and resampled spectra of selected samples with those extracted from the Hyperion subset image (Fig. 10).

Furthermore, a subtle displacement in the unique absorption properties of these minerals was detected when comparing these processed ASD and Hyperion extracted spectra with U.S. Geological Survey oxide (hematite, goethite,) and clay (kaolinite) spectra at around 0.49, 0.56, 0.88, and 2.203  $\mu\text{m}$ , respectively (Fig. 10). Thus, the presence of hematite and goethite minerals can explain the detected absorption feature at around 0.52  $\mu\text{m}$  in both ASD recorded spectra and the extracted ones from the Hyperion image. XRD results confirmed that oxide and clay minerals are present in all selected samples.

### 4.3 Characterization of Iron Oxide and Clay Minerals

The Hyperion image was utilized to construct the band ratio technique ferric and ferrous iron index, which was then used for delineating zones showing the subsurface existence of iron ore.<sup>40,54–56,74,75</sup> NDVI's and NDWI's goal is to hide heavy vegetation and water regions and turn the pixels with high vegetation and water values in black color, which means there is

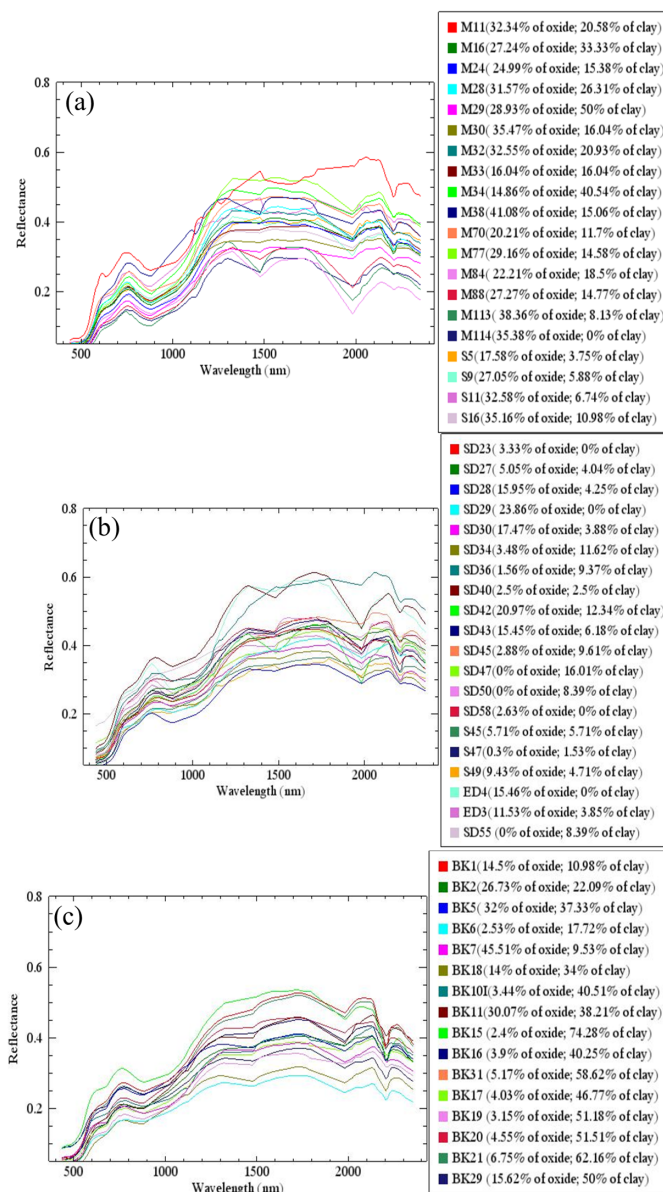


**Fig. 9** ASD soil spectra taken from the three sites with their corresponding mean abundance (%) of iron and clay minerals: (a) reflectance curves of “Tamera” soil samples, (b) reflectance curves of “Sidi Driss” soil samples, and (c) reflectance curves of “Boukhchiba” soil samples.

no value. A water mask also was generated according to a visual inspection and field truth. In particular, Boukhchiba is a mine bonded to a dense forest in the northern area, so when we replicate the mask of vegetation, the northern zone turned black. The two black holes located in Sidi Driss are small lakes. The spatial distribution of clay mineral and iron oxide classes is determined and given in Table 2. Based on the same threshold level for iron oxide and clay ratio bands, it was discovered that the iron oxide ratio band has the highest value of the total district area with 1.707% in the image sequence. Most of the oxides and iron minerals are geographically distributed in the Tamera mine, whereas clay minerals are concentrated in the Boukhchiba mine.

#### 4.4 Iron Oxide and Clay Mineral Mapping

The SFF algorithm was conducted on the subset of the Hyperion data using extracted endmember spectra. The scene extracted spectra were compared with their corresponding measured

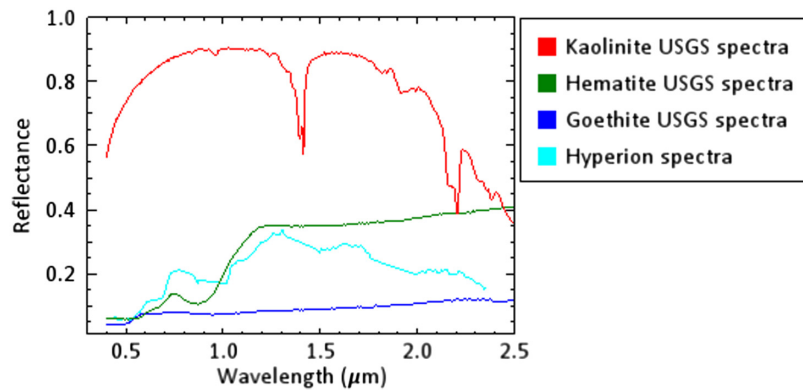


**Fig. 10** Comparison between the extracted spectrum from Hyperion and the U.S. Geological Survey kaolinite, hematite, and goethite re-sampled spectra.

**Table 2** Class distribution summary of clay and iron oxide minerals of the Hyperion full scene 360 × 250 × 1 pixels.

Class distribution summary		Full scene: 187,200 points (360 × 520 × 1)		
		% of the total district area	Pixels	Cover area (m <sup>2</sup> )
Oxide	Unclassified	98.293	184,005	165,372,437.3505
	Ratio ( <i>b</i> 23/ <i>b</i> 13)	1.707	3195	2,871,470.5434
Clay	Unclassified	98.329	184,072	165,432,652.8518
	Ratio ( <i>b</i> 134 × <i>b</i> 138/ <i>b</i> 148 <sup>2</sup> )	1.671	3128	2,811,255.0422

spectra before processing, thus serving as ground truth (Fig. 11). Furthermore, a subtle displacement in the unique absorption properties of these minerals was detected when comparing these properties, which were measured by ASD, and the endmembers spectra extracted from Hyperion oxide (hematite, goethite,) and clay (kaolinite) spectra at around 0.49, 0.56, 0.88, and 2.203 μm, respectively (Fig. 11). Thus, the presence of oxide minerals can explain the detected absorption feature at around 0.52 and 0.89 μm in both ASD recorded spectra and the extracted ones from the Hyperion image. Moreover, the clay minerals class extracted from the Hyperion and measured by ASD shows a strong absorption peak at around 2.203 μm.

Iron oxide (hematite and goethite) and clay (kaolinite and illite) mineral distributions are showed in the resulting maps after SFF method-based Hyperion processing (Figs. 12 and 13). As a result of the Hyperion image processing, iron oxide (hematite and goethite) was identified

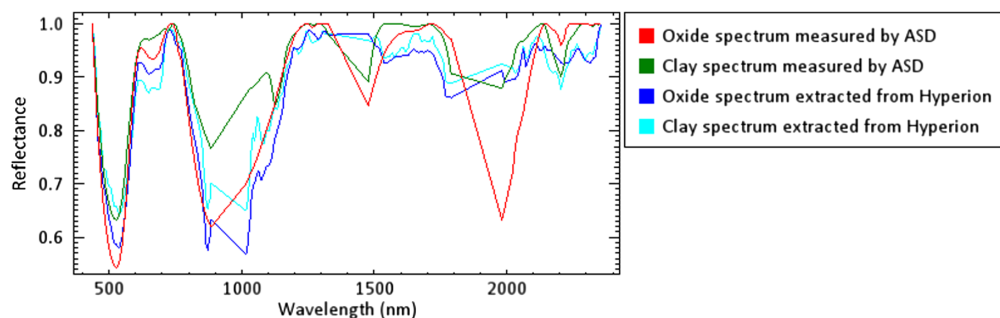


**Fig. 11** Comparison between the extracted spectra from the image and those measured by the ASD for oxides and clays.

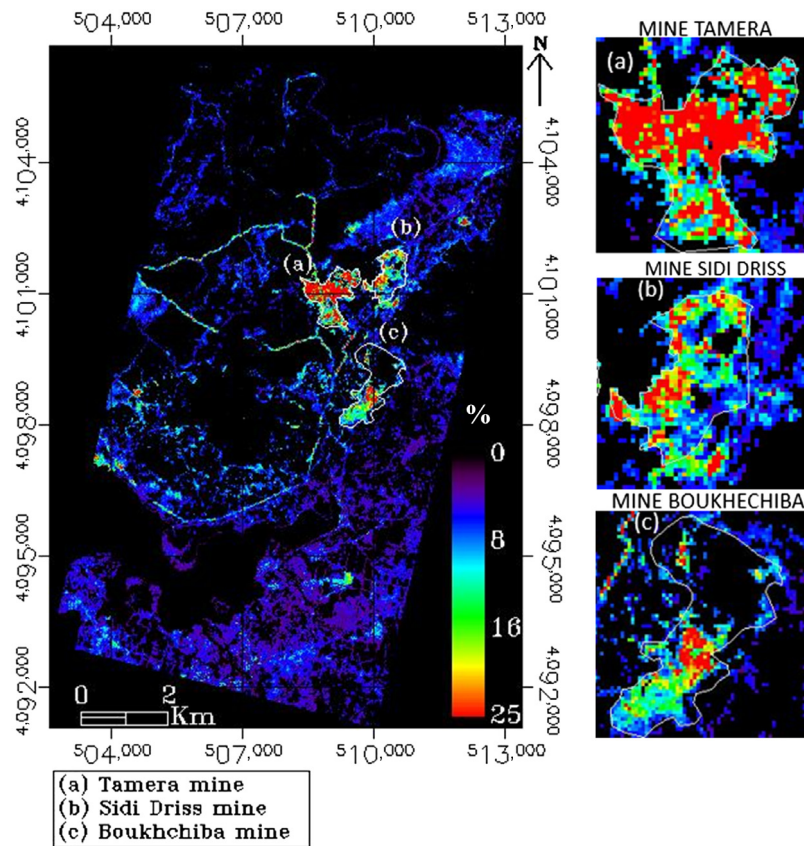


**Fig. 12** Maps showing the distribution of iron oxide minerals resulting from the Hyperion image processing using the SFF algorithm. The full scene ( $360 \times 250 \times 1$  pixels) and the zoomed images of the three sites of Tamera ( $54 \times 54 \times 1$  pixels), Sidi Driss ( $44 \times 73 \times 1$  pixels), and Boukhchiba ( $58 \times 71 \times 1$  pixels) (1. Raget Ouled Mariem, 2. Kef Salem, and 3. West sector of Boukhchiba).

in the three studied areas with high concentration in the Tamera region, where such minerals are dominant. However, the Boukhchiba and Sidi Driss sites show low and very low abundances of iron oxide minerals, respectively (Fig. 12). Iron oxide amounts of 28.52%, 8.61%, and 14.19% were estimated for the Tamera, Sidi Driss, and Boukhchiba mines, respectively. The primary edge breccia Raget Ouled Mariem, located to the North of Boukhchiba, and Kef Salem, situated in its central-eastern part, have shown considerable values of iron oxide at around 15.6% and 16.36%, respectively. Some other pixels, not belonging to zones with dense vegetation and that are attributed to interior secondary breccias, revealed moderate values of iron oxide at around 9.22%.

These results converge with those determined by the mineralogical analysis through XRD. The significant amounts of iron oxides, which were revealed by the resulting map and considered to be economically profitable, suggest that Boukhchiba site could be re-exploited.

Moreover, band ratio results revealed similar geographical distribution of iron oxide mineral contents, particularly high in the Tamera site, moderate in the Boukhchiba site, and low in the Sidi Driss site [Fig. 7(a)].

According to the resulting map, clay minerals (kaolinite and illite) were detected with a higher grade in the Boukhchiba site. A lower grade was, however, revealed in the Tamera and Sidi Driss sites. The determined amounts of clays ranged from 6.95% to 57.14% in Boukhchiba and less than 56.59% in Tamera and Sidi Driss. Clay estimated contents are close to those measured by XRD analysis, with mean values at 31.19% compared with 16.38% in Boukhchiba, 5.83% compared with 15.1% for Sidi Driss, and 17.47% compared with 15.63% for Tamera. A convergence between clay maps and band ratio results were found, thus confirming their significance.

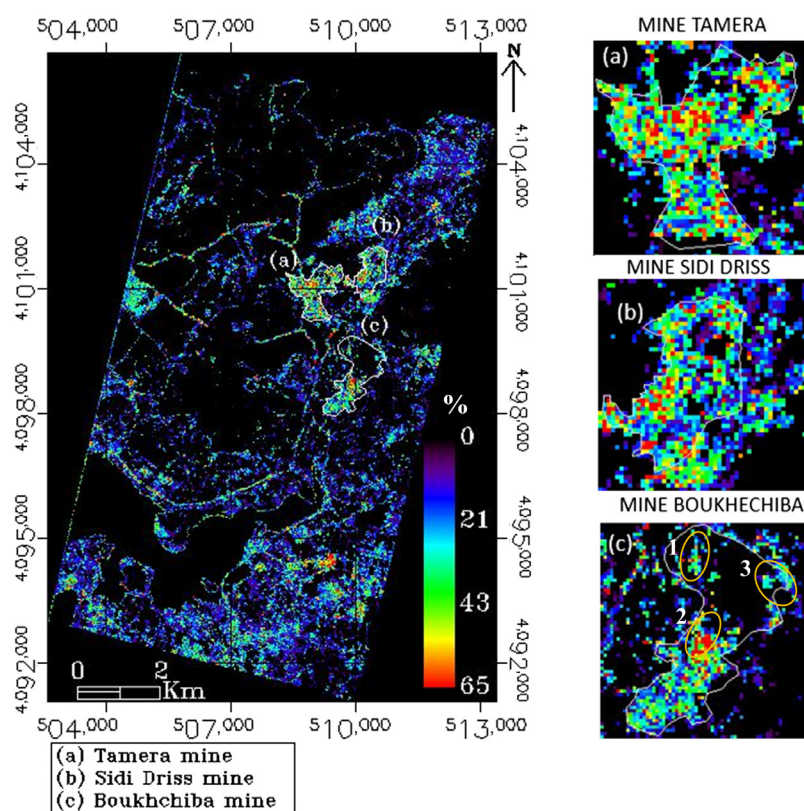


**Fig. 13** Maps showing the distribution of clay minerals resulting from the Hyperion image processing using the SFF algorithm. The full scene ( $360 \times 250 \times 1$  pixels) and the zoomed images of the three sites of Tamera ( $54 \times 54 \times 1$  pixels), Sidi Driss ( $44 \times 73 \times 1$  pixels), and Boukhchiba ( $58 \times 71 \times 1$  pixels) (1. Raget Ouled Mariem, 2. Kef Salem, and 3. West sector of Boukhchiba).

## 4.5 Iron Oxide and Clay Map Validation

### 4.5.1 Validation using kriging maps

One of the most often used methods for quantifying classification accuracy is the kriging method.<sup>76,77</sup> A normal krige model is applied to calculate, or rather estimate, the global estimation variances, as well as to identify the kriging weights in the local estimation.<sup>78</sup> In this context, we used the XRD results to generate kriging maps for Iron oxide and clay maps validation.

The ordinary kriging model was estimated by the variance of iron oxide minerals in the three sites (Fig. 14). The highlighted region of high iron oxide grades was the same for both the normal kriging method and the SFF classification findings. High oxide amounts were located particularly in the eastern, western, and central areas of Tamera, with over 20%, which overlaid with the greatest value pixels of the SFF classification map, with an amount estimated at about 48.41% [Fig. 14(a)]. They were, however, revealed in the north of Sidi Driss with maximum values at around 31.51% in the SFF classification map [Fig. 14(b)]. The highest pixels of iron oxide grade were located specifically in the central area of the Boukhchiba mine with a maximum value at around 35.48% in the SFF classification map [Fig. 14(c)].

The variability of clay mineral contents in the three sites was also evaluated using the standard kriging model. The spatial distribution showed agreement between the normal kriging map and the SFF classification results. Pixels showing higher amounts were located particularly in the central and northern areas of Tamera's reddish Mio-Pliocene formation with estimated amounts of more than 20%, which was overlaid with the greatest value pixels of clay results from SFF classification with an amount at around 56.59% [Fig. 15(a)]. Furthermore, the SFF classification map of the Sidi Driss showed moderate to low values of clay contents, with a maximum of 15.96%, which converges with the kriging map results [Fig. 15(b)]. According to resulting kriging and SFF maps, Boukhchiba seems to be the site with the highest grade of clay minerals, with a

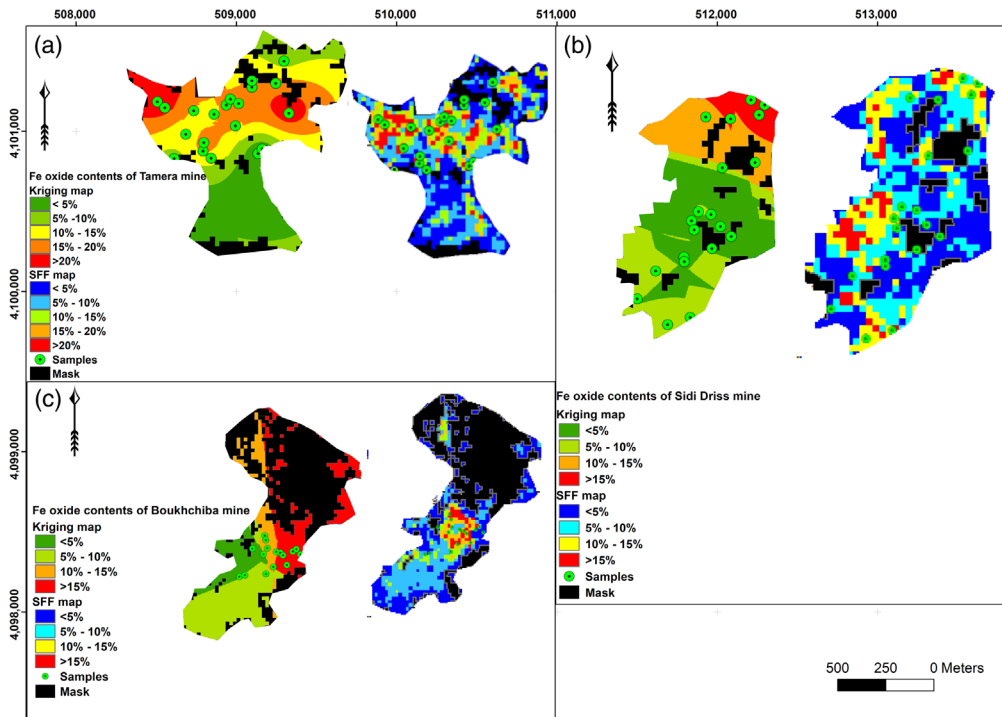


**Fig. 14** Kriging maps showing the distribution of iron oxide minerals using XRD abundance results in the three sites (56 samples): (a) Tamera (20 samples), (b) Sidi Driss (20 samples), and (c) Boukhchiba (16 samples).

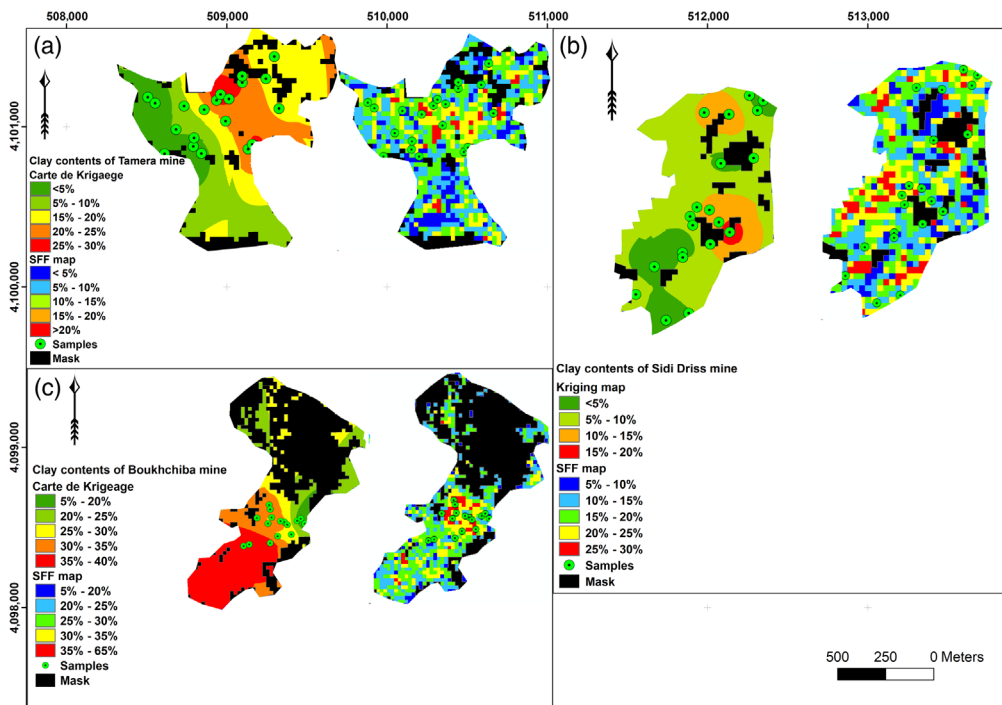


**Fig. 15** Kriging maps showing the distribution of clay minerals using XRD abundance results in the three sites (56 samples): (a) Tamera (20 samples), (b) Sidi Driss (20 samples), and (c) Boukhchiba (16 samples).

maximum value of 41.09% and of 57.14%, respectively. [Fig. 15(c)]. The convergence between the kriging and SFF classification results confirmed the usefulness of the proposed approach for mapping Iron oxide and clay minerals in an attempt to delineate the spatial distribution of Fe ores in the three studied sites. An accurate map of the mineralization will be of utmost interest for selecting the judicious procedure for extracting Fe ores to minimize the impacts on environment.

#### 4.5.2 Validation using test samples

A total of 20 soil samples were randomly selected for the Tamera and Sidi Driss areas, and 16 samples were selected for the Boukhchiba mine. The calculated coefficient of correlation between measured iron oxide abundances by XRD analysis and their corresponding values, estimated from SFF-based Hyperion processing, revealed a relative important convergence between measured and estimated abundances in the Tamera and Boukhchiba mines ( $R^2 = 0.644$  and  $R^2 = 0.619$ , respectively). There was less convergence between measured and estimated oxide abundances in the Sidi Driss mine, as revealed by the  $R^2$  of 0.543. For clay minerals, a strong correlation was revealed by an  $R^2$  coefficient equal to 0.715, particularly in the Tamera mine site (Fig. 16). Less important  $R^2$  coefficients were calculated for the Sidi Driss and Boukhchiba mine

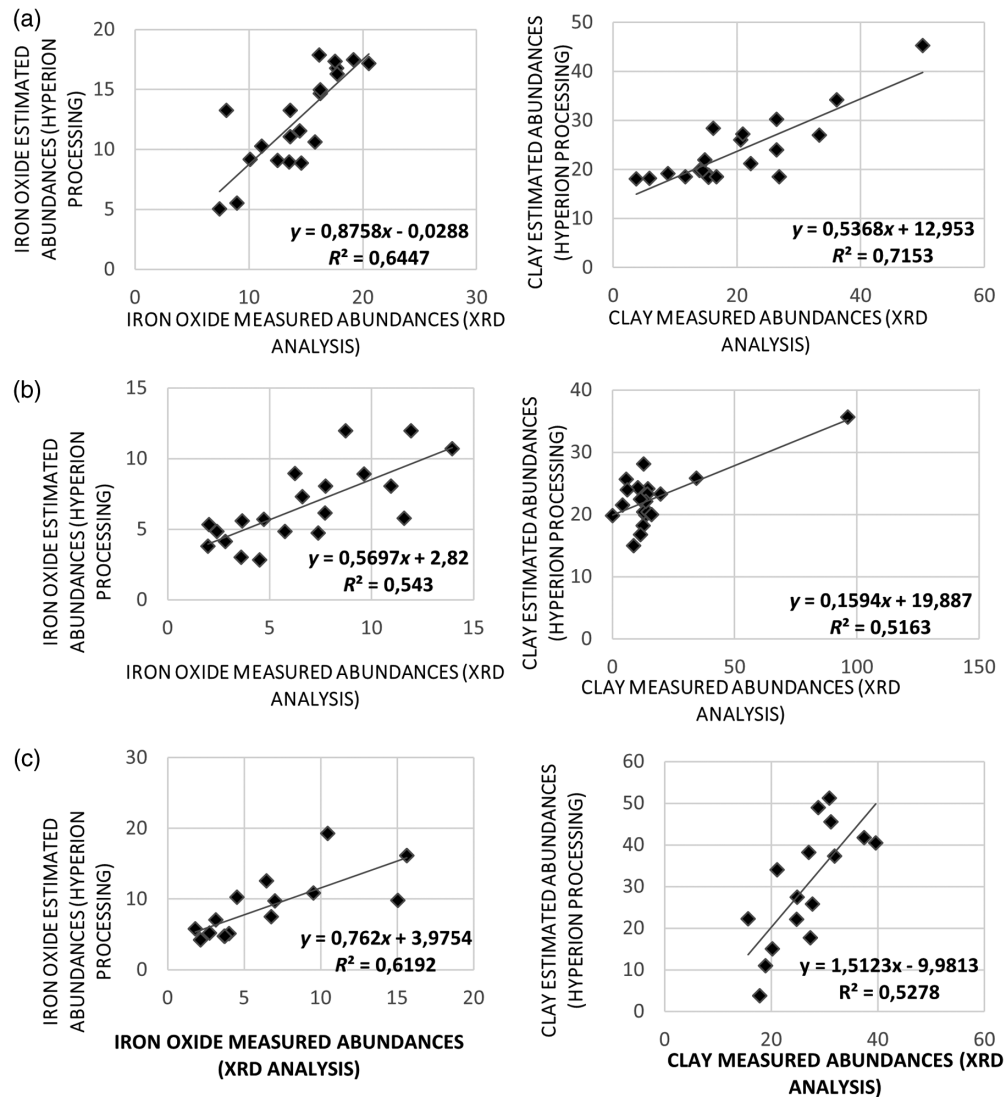


**Fig. 16** Correlation between XRD measured abundances and estimated abundances from SFF-based Hyperion processing for Iron oxide and clay minerals of the three study sites: (a) Tamera, (b) Sidi Driss, and (c) Boukhchiba.

sites, equal to 0.516 and to 0.527, respectively. These correlation values indicate that Hyperion processing results were highly converged with those measured by XRD laboratory analysis for iron oxides and clays in ore deposits. This study has shown that the SFF-based methodology can be used successfully for iron ore mapping and grade assessment using Hyperion data.

## 5 Conclusion

This study aimed to explore Iron oxide mineralization in a particular nappe zone using multiscale VNIR/SWIR and EO-1 Hyperion image data. Thus, a methodological approach was conducted based on the SFF classification and reflectance spectroscopy. A total of 65 soil samples were selected from the three studied sites, and *in situ* reflectance spectra were taken from the same point locations. The mineralogical composition of each sample was identified through the XRD analysis, which was used for the validation of the resulting mineral maps. In particular, Iron oxide and clay maps were generated based on the SFF classification method and using Hyperion scene-extracted spectra. All extracted spectra were compared with the ASD measured spectra before the classification step.

*In situ* reflectance measurement revealed the presence of oxide and hydroxide minerals with absorption features of approximately 520 and 890 nm. Moreover, clays were depicted with a principal absorption peak in the SWIR region at around 2200 nm. These results converged with XRD results, which confirmed the presence of oxides (hematite and goethite) and clays (kaolinite and illite).

The generated SFF maps have shown a dominance of oxides in the Tamera mine and lower grades in the Boukhchiba and Sidi Driss mine sites, with estimated contents of around 48.41%, 35.48%, and 31.51%, respectively. According to the results, clays were identified with high content in the Boukhchiba mine with 57.14%. Less important contents were determined in the Tamera and Sidi Driss mines considering the revealed amounts at about 56.59% and 37.92%, respectively. These results perfectly highlighted the Iron oxide and clay areas, which were also enhanced based on band ratio method. Both oxide and clay maps, generated from the SFF classification, were validated using XRD analysis. A first validation was conducted using the generated kriging maps, using XRD results, to validate maps spatially. A significant distribution similarity was revealed between the kriging map and SFF map for the Tamera mine site. The second validation step was conducted through the comparison between the estimated contents with those measured by XRD analysis of each test sample. In particular, the oxide map that was generated for Tamera mine showed the best correlation coefficient, up to 0.6. The convergence between XRD and SFF classification results confirmed the usefulness of the proposed approach for mapping Iron oxide and clay minerals in an attempt to delineate the spatial distribution of Fe ores in the three studied sites. Moreover, other significant amounts of iron oxides, which were revealed by the resulting map, particularly in the northern and central-eastern parts of the abandoned Boukhchiba site as well as some zones far from the three studied sites, are considered to be economically profitable and thus could be re-exploited. An accurate map of the mineralization will be of utmost interest for selecting the judicious procedure for extracting Fe ores to minimize the impacts on environment. This study has shown that the SFF-based methodology can be successfully used for iron ore mapping and grade assessment using Hyperion data.

## References

1. C. Gottis, "Les gisements de fer en Tunisie," C.R. XIX<sup>ème</sup> symposium sur le fer (1952).
2. S. Decrée et al., "Pb–Zn mineralization in a Miocene regional extensional context: The case of the Sidi Driss and the Douahria ore deposits (Nefza mining district, northern Tunisia)," *Ore Geol. Rev.* **34**, 285–303 (2008).
3. R. Bouzouada, "Géologie, minéralogies et paragenèses es gites de fer du district des Nefza. Réparation des sulfures et des impuretés," mémoire D.E.A., en géologie, FST., p. 77 (1992).
4. A. Vural, I. Akpınar, and F. Sipahi, "Mineralogical and chemical characteristics of clay areas, Gümüşhane Region (NE Turkey), and their detection using the Crósta Technique with Landsat 7 and 8 Images," *Nat. Resour. Res.* **30**, 3955–3985 (2021).

5. Vural, Ö. Çorumluoglu and İ. Asrı, "Remote sensing technique for capturing and exploration of mineral deposit sites in Gumushane metallogenic province, NE Turkey," *J. Geol. Soc. India* **90**(5), 628–633 (2017).
6. S. Gabr, A. Ghulam, and T. Kusky, "Detecting areas of high-potential gold mineralization using ASTER data," *Ore Geol. Rev.* **38**, 59–69 (2010).
7. W. Bouzidi, N. Mezned, and S. Abdeljaouad, "Hyperspectral reflectance spectroscopy and x-ray diffraction for iron minerals characterization in northern Tunisia," *Proc. SPIE* **10790**, 107901Q (2018).
8. W. D. Sinclair, "Porphyry deposits. Geological survey of Canadapp. 14. Soheili, M., 1981. Geological Map of Anar, 1:250 000 Map," Geological Survey of Iran Publication, Tehran (2004).
9. N. Mezned et al., "Cascade sub-pixel unmixing of aster SWIR data for mapping alteration minerals in Tamra Sidi-Driss SITE, NW Tunisia," in *IEEE Int. Geosci. and Remote Sens. Symp.* (2017).
10. E. Papp and T. Cudahy, "Hyperspectral remote sensing, geophysical and remote sensing methods for regolith exploration," CRCLEME open file report, 144, pp. 13–21 (2002).
11. J. Wang and J. Zhang, "Study on clay alteration information extraction in vegetation coverage based on MTMF," in *Int. Conf. Remote Sens., Environ. and Transp. Eng.*, pp. 8526–8529 (2011).
12. J. C. Mars and L. C. Rowan, "Spectral assessment of new ASTER SWIR surface reflectance data products for spectroscopic mapping of rocks and minerals," *Remote Sens. Environ.* **114**(9), 2011–2025 (2010).
13. M. H. Zadeh and M. H. Tangestani, "Mapping alteration minerals using sub-pixel unmixing of ASTER data in the Sarduiyeh area, southeastern Kerman Iran," *Int. J. Digital Earth* **4**(6), 487–504 (2011).
14. H. Ranjbar, F. Masoumi, and E. J. M. Carranza, "Evaluation of geophysics and spaceborne multispectral data for alteration mapping in the Sarcheshmeh mining area Iran," *Int. J. Remote Sens.* **32**(12), 3309–3327 (2011).
15. R. Amer, T. Kusky, and A. Mezayen, "Remote sensing detection of gold related alteration zones in Um Rus area, Central Eastern Desert of Egypt," *Adv. Space Res.* **49**(1) 121–134 (2012).
16. E. Bedini, "Mineral mapping in the Kap Simpson complex, central East Greenland, using HyMap and ASTER remote sensing data," *Adv. Space Res.* **47**, 60–73 (2011).
17. Y. Yamaguchi et al., "Overview of advanced spaceborne thermal emission and reflection radiometer (ASTER)," *IEEE Trans. Geosci. Remote Sens.* **36**, 1062–1071 (1998).
18. F. A. Kruse, A. B. Lefkoff, and J. B. Dietz, "Expert system-based mineral mapping in northern death valley, California/Nevada, using the airborne visible/infrared imaging spectrometer (AVIRIS)," *Remote Sens. Environ.* **44**(2–3), 309–336 (1993).
19. M. C. De Morais, P. P. M. Junior, and W. R. Paradella, "Multi-scale approach using remote sensing images to characterize the iron deposit N1 influence areas in Carajás Mineral Province (Brazilian Amazon)," *Environ Earth Sci.* **66**, 2085–2096 (2012).
20. F.A. Kruse, "Regional mapping along the Colorado river front range from FT Collins to Denver using the airborne visible/infrared imaging spectrometer (AVIRIS)," *12th Int. Conf. Appl. Geol. Remote Sens.*, Denver, Colorado (1997).
21. F. A. Kruse and S. L. Perry, "Mineral mapping using simulated worldview-3 short-wave-infrared imagery," *Remote Sens.* **5**(6), 2688–2703 (2013).
22. M. H. Zadeh et al., "Mineral exploration and alteration zone mapping using mixture tuned matched filtering approach on ASTER data at the central part of Dehaj-Sarduiyeh copper belt SE Iran," *IEEE Sel Top. Appl. Earth Obs. Remote Sens.* **7**, 284–289 (2014).
23. A. Moghtaderi, F. Moore, and A. M. Zadeh, "The application of advanced spaceborne thermal emission and reflection (ASTER) radiometer data in the detection of alteration in the Chadormalu paleocrater, Bafq region, Central Iran," *J. Asian Earth Sci.* **30**(2), 238–252 (2007).
24. X. Zhang, M. Pazner, and N. Duke, "Lithologic and mineral information extraction for gold exploration using ASTER data in the south Chocolate Mountains (California)," *ISPRS J. Photogramm. Remote Sens.* **62**, 271–282 (2007).

25. A. B. Pour and M. Hashim, "Identification of hydrothermal alteration minerals for exploring of porphyry copper deposit using ASTER data, SE Iran," *J. Asian Earth Sci.* **42**(6), 1309–1323 (2011).
26. S. K. Raj et al., "Iron oxides mapping from EO-1 Hyperion data," *J. Geol. Soc. India* **86**(16), 717–725 (2015).
27. D. F. Ducart et al., "Mapping iron oxides with Landsat-8/OLI and EO-1/Hyperion imagery from the Serra Norte iron deposits in the Carajás Mineral Province, Brazil," *Braz. J. Geol.* **46**(3), 331–349 (2016).
28. F. Van Deer Meer and S. De Jong, "Multi- and hyperspectral geologic remote sensing: a review," *Int. J. Appl. Earth Obs. Geoinf.* **14**(1), 112–128 (2012).
29. G. R. Hunt, "Spectral signatures of particulate minerals in the visible and near infrared," *Geophysics*, **42**, 501–513 (1977).
30. G. R. Hunt and P. Ashley, "Spectra of altered rocks in the visible and near infrared," *Econ. Geol.* **74**, 1613–1629 (1979).
31. T. J. Cudahy et al., "The performance of the satellite-borne Hyperion hyperspectral VNIR-SWIR imaging system for mineral mapping at Mount Fitton, South Australia," in *Scanning Present and Resolving Future. Proc. IEEE Int. Geosci. and Remote Sens. Symp. (Cat. No.01CH37217)*, IEEE (2001).
32. J. K. Crowley, B. E. Hubbard, and J. C. Mars, "Analysis of potential debris flow source areas on Mount Shasta, California, by using airborne and satellite remote sensing data," *Remote Sens. Environ.* **87**, 345–358 (2003).
33. B. Hubbard, J. Crowley, and D. Zimelman, "Comparative alteration mineral mapping using visible to shortwave infrared (0.4 – 2.4  $\mu\text{m}$ ) Hyperion, ALI, and ASTER imagery," *IEEE Trans. Geosci. Remote Sens.* **41**(6), 1401–1410 (2003).
34. F. A. Kruse, J. W. Boardman, and J. F. Huntigton, "Comparison of airborne Hyperspectral data and EO-1 Hyperion for mineral mapping," *IEEE Trans. Geosci. Remote Sens.* **41**(6), 1388–1400 (2003).
35. B. Hubbard and J. K. Crowley, "Mineral mapping on the Chilean–Bolivian Altiplano using co-orbital ALI, ASTER and Hyperion imagery: data dimensionality issues and solutions," *Remote Sens. Environ.* **99**(1–2), 173–186 (2005).
36. R. Gersman et al., "Mapping of hydrothermally altered rocks by the EO-1 Hyperion sensor, Northern Danakil Depression, Eritrea," *Int. J. Remote Sens.* **29**, 3911–3936 (2008).
37. B. T. San and M. L. Suzen, "Evaluation of different atmospheric correction algorithms for EO-1 Hyperion imagery," *Int. Arch. Photogramm. Remote Sens. Spat. Inf. Sci.* **XXXVIII**(8), 392–397 (2010).
38. B. A. Pour and M. Hashim, "The Earth Observing-1 (EO-1) satellite data for geological mapping, southeastern segment of the Central Iranian Volcanic Belt, Iran," *Int. J. Phys. Sci.* **6**(33), 7638–7650 (2011).
39. C. A. Bishop, J. G. Liu, and P. J. Mason, "Hyperspectral remote sensing for mineral exploration in Pulang, Yunnan Province China," *Int. J. Remote Sens.* **32**(9), 2409–2426 (2011).
40. A. Sengupta et al., "Identification and mapping of high-potential iron ore alteration zone across Joda, Odisha using ASTER and EO-1 Hyperion data," *J. Spat. Sci.* **64**, 491–514 (2018).
41. M. Thangavelu, S. Shanmugam, and A. K. Bhattacharya, "Hyperspectral radiometry to quantify the grades of iron ores of Noamundi and Joda Mines, eastern India," *J. Indian Soc. Remote Sens.* **39**, 473–483 (2011).
42. T. Magendran and S. Sanjeevi, "Hyperion image analysis and linear spectral unmixing to evaluate the grade of iron ores in parts of Noamundi, eastern India," *Int. J. Appl. Earth Obs. Geoinf.* **26**, 413–426 (2014).
43. P. Gopinathan, S. P. Mohan, and T. Magendran, "Spectral remote sensing and digital processing of satellite images for characterizing the iron ores of Kanjamalai, Godumalai and Nainarmalai, India—a case study," *Int. J. Sci. Res.* **4**(14), 3125–3130 (2015).
44. M. H. Tangestani et al., "Spectral characterization and ASTER-based lithological mapping of an ophiolite complex: a case study from Neyriz ophiolite, SW Iran," *Remote Sens. Environ.* **115**(9), 2243–2254 (2011).

45. L. Negra, "Pétrologie, minéralogie et géochimie des minéralisations et des roches encaissantes des bassins associés aux structures tectoniques et magmatiques de l'oued Bélif et du Jbal Haddada (Nord des Nefza, Tunisie septentrionale)," Thèse 3ème cycle, Paris (1987).
46. M. Dermech, "Le complexe de l'oued Bélif-Sidi Driss (Tunisie septentrionale) hydrothermalisme et métallogénie," p. 354 (1990).
47. S. Decrée et al., "The Oued Belif Hematite-Rich Breccia: a Miocene iron oxide Cu-Au-(U-REE) deposit in the Nefza Mining District, Tunisia," *Econ. Geol.* **108**(6), 1425–1457 (2013).
48. L. Berthon, "L'industrie minérale en Tunisie," (1922).
49. H. Rouvier, "Carte géologique de Tunisie au 1/50000," Nefza, feuille n°10 (1987).
50. P. Batik, "Carte géologique de Tunisie au 1/50000," Hédile, feuille n°11 (1980).
51. L. Liao et al., "Performance characterization of the Hyperion imaging spectrometer instrument," *Proc. SPIE* **4101**, 22–26 (2000).
52. S. G. Ungar et al., "Overview of the earth observing one (EO-1) mission," *IEEE Trans. Geosci. Remote Sens.* **41**, 1149–1159 (2003).
53. P. Barry, "EO-1 Hyperion science data user's guide," level 1\_B, TRW space, Defense & Information Systems (2001).
54. M. D. Hankan, "Mineral composite assessment of Kelkit River Basin in Turkey using remote sensing," *J. Earth Syst. Sci.* **118**(16), 701–710 (2012).
55. M. Bodruddoza and F. Yasuhiro, "Mapping hydrothermal altered mineral composite using LANDSAT 7 ETM+ image in and around Kujū volcano, Kyushu, Japan," *J. Earth Syst. Sci.* **121**(14), 1049–1057 (2012).
56. D. M. Sherman, "Electronic spectra of Fe<sup>3+</sup> oxides and oxide hydroxides in the near IR to near UV," *Am. Mineralog.* **70**, 1262–1269 (1995).
57. J. Inzana et al., "Supervised classifications of Landsat TM band ratio images and Landsat TM band ratio image with radar for geological interpretations of central Madagascar," *J. African Earth Sci.* **37**(1-2), 59–72 (2003).
58. K. N. Priyadarshini et al., "Comparison and evaluation of dimensionality reduction techniques for hyperspectral data analysis," *Proceedings* **24**, 6 (2019).
59. A. A. Green et al., "A transformation for ordering multispectral data in terms of image quality with implications for noise removal," *IEEE Trans. Geosci. Remote Sens.* **26**, 65–74 (1988).
60. J. R. Jenson, *Introductory Digital Image Processing: A Remote Sensing Perspective*, Pearson, Prentice Hall, Upper Saddle River (2005).
61. T. Uezato et al., "A novel endmember bundle extraction and clustering approach for capturing spectral variability within endmember classes," *IEEE Trans. Geosci. Remote Sens.* **54**, 6712–6731. (2016).
62. B. Somers et al., "Automated extraction of image-based endmember bundles for improved spectral unmixing," *IEEE J. Sel. Top. Appl. Earth Obs. Remote Sens.* **5**(2), 396–408 (2012).
63. C. A. Bateson, G. P. Asner, and C. A. Wessman, "Endmember bundles: a new approach to incorporating endmember variability into spectral mixture analysis," *IEEE Trans. Geosci. Remote Sens.* **38**(2), 1083–1094 (2000).
64. M. Xu et al., "Archetypal analysis for endmember bundle extraction considering spectral variability," in *9th Workshop Hyperspectral Image and Signal Process.: Evol. Remote Sens.*, Amsterdam, pp. 23–26 (2018).
65. J. W. Boardman, "Automated spectral unmixing of AVIRIS data using convex geometry concepts," in *Summaries Annu. JPL Airborne Geosci. Workshop*, JPL Publication 93-26, Jet Propulsion Laboratory, Pasadena, CA, Vol. 1, pp. 11–14 (1993).
66. J. W. Boardman, F. A. Kruse, and R. O. Green, "Mapping target signatures via partial unmixing of AVIRIS data," in *Summaries, Fifth JPL Airborne Earth Science Workshop*, JPL Publication 95-1, Vol. 1, pp. 23–26 (1995).
67. F. A. Course, J. W. Boardman, and J. F. Huntington, "Comparison of airborne hyperspectral data and EO-1 Hyperion for mineral mapping," *IEEE Trans. Geosci. Remote Sens.* **41**(6), 1388–1400 (2003).

68. S. Perry, "Spaceborne and airborne remote sensing systems for mineral exploration- case histories using infrared spectroscopy, infrared spectroscopy in geochemistry," in *Exploration Geochemistry, and Remote Sensing*, P. Ing, M. Ramsey, and G. Swayze, Éds., pp. 227–240, Mineralogical Association of Canada, London (2004).
69. H. Harris, "Continuum removal," *Geospatial solutions*, retrieved (2017).
70. J. D. Wolfe and S. R. Black, "Hyperspectral analytics in ENVI target detection and spectral mapping methods," Harris Cooperation (2018).
71. R. N. Clark, G. A. Swayze, and A. Gallagher, "Mapping the mineralogy and lithology of Canyonlands, Utah with imaging spectrometer data and the multiple spectral feature mapping algorithm," in *Summaries Third Annu. JPL Airborne Geosci.* (1992).
72. F. Van der Meer, "Analysis of spectral absorption features in hyperspectral imagery," *Int. J. Appl. Earth Obs. Geoinf.* **5**(1), 55–68 (2004).
73. P. Sobron et al., "Natural Fe-bearing oxides and sulfates from the Rio Tinto Mars analog site: critical assessment of VNIR reflectance spectroscopy, laser Raman spectroscopy, and XRD as mineral identification tools," *Am. Mineralog.* **99**(7), 1199–1205 (2014).
74. A. F. Alasta, "Using remote sensing data to identify iron composite in central western Libya," in *Int. Conf. Emerging Trends Comput. and Image*, Bangkok (2011).
75. T. L. Hung, "Application of band ratio method to detect iron oxide, clay minerals and ferrous minerals," *Mining Ind. J.* **4**, 19–24 (2013).
76. R. G. Congalton, "Accuracy assessment and validation of remotely sensed and other spatial information," *Int. J. Wildland Fire* **10**, 321–328 (2001).
77. J. Cohen, "A coefficient of agreement for nominal scales," *Educ. Psychol. Meas.* **20**, 37–46 (1960).
78. M. Mazari, "Geostatistical study of mining resources: example of a mine under evaluation" (2012).

**Wejden Bouzidi** is a PhD student at the Faculty of Sciences of Tunis, the University of Tunis El Manar. Her research focuses on characterization of iron mineral deposit in the north of Tunisia using hyperspectral remote sensing tools. She received her MSc degree in earth sciences from the same university in 2016.

**Nouha Mezned** is a research professor in the LRME Laboratory at the Faculty of Sciences of Tunis and an assistant professor in the Higher Institute of Preparatory Studies in Biology and Geology at the University of Carthage. She received her PhD in geology from the FST in 2010. Her main research activities are in the field of protecting the mining environment. She is interested also in ore exploration and mapping. Specialized in remote sensing and GIS, she has undertaken research on the spectral characterization of waste and the mapping of contaminated soils. Several of her research endeavors have dealt with phosphate and iron ore exploration and mapping.

**Saâdi Abdeljaouad** is a professor in the Faculty of Sciences of Tunis at the University of Tunis El Manar since 1991. He received his engineering geologist degree in 1981 from the French Petroleum Institute, his master's degree from the Louis Pasteur Institute in Strasbourg in 1979, and his PhD in 1983 and a Doctorate of State Es Sciences in 1991, both from the FST. He has been a research professor at FST since 1980, was an expert to the court of first instance of Tunis, and has been an expert of insurance since 1995. He was the director of the LRME laboratory from 2001 to 2014.